# Inner crust of neutron stars with mass-fitted Skyrme functionals

J. M. Pearson,[1] N. Chamel,[2] S. Goriely,[2] and C. Ducoin[3,4]
[1]*Département de Physique, Université de Montréal, Montréal, Québec H3C 3J7, Canada*
[2]*Institut d'Astronomie et d'Astrophysique, CP-226, Université Libre de Bruxelles, 1050 Brussels, Belgium*
[3]*CFC, Department of Physics, University of Coimbra, P3004-516 Coimbra, Portugal*
[4]*Institut de Physique Nucléaire de Lyon, CNRS/IN2P3, Université Claude Bernard Lyon 1, Villeurbanne, France*
(Received 22 August 2011; published 11 June 2012)

The equation of state and composition of the inner crust of neutron stars at zero temperature are calculated, using the $T = 0$ version of the temperature-dependent extended Thomas-Fermi plus Strutinsky integral method, for each of a family of three functionals based on Skyrme-type forces BSk19, BSk20, and BSk21, which are characterized by different degrees of symmetry-energy stiffness, and also for the SLy4 functional. We also solve the Tolman-Oppenheimer-Volkoff equations to calculate the distribution of mass within the inner crust. Qualitatively similar results are found for all four functionals, and in particular the number of protons per Wigner-Seitz cell is in all cases equal to 40 throughout the inner crust.

DOI: 10.1103/PhysRevC.85.065803 PACS number(s): 26.60.Gj, 04.40.Dg, 21.10.Dr, 21.30.−x

## I. INTRODUCTION

We recall that three distinct regions can be recognized in a neutron star: a locally homogeneous core and two concentric shells characterized by different inhomogeneous phases [1,2]. The outermost of the shells, the "outer crust," consists of an electrically neutral lattice of nuclei and electrons. At the surface of the star only nuclei that are stable under natural terrestrial conditions are found (in fact, under the assumption of "cold catalyzed matter," i.e., nuclear and $\beta$ equilibrium at temperature $T = 0$, only $^{56}$Fe will be found), but on moving toward the interior the increasing density leads to the appearance of nuclei that are more and more neutron rich, until at a mean local density $\bar{n}$ of around $2.5 \times 10^{-4}$ nucleons fm$^{-3}$ ($4.2 \times 10^{11}$ g cm$^{-3}$) neutron drip sets in. This marks the transition to the "inner crust," an inhomogeneous assembly of neutron-proton clusters and unbound neutrons, neutralized by an essentially uniform electron gas. By the point where the mean density has risen to about two thirds of the density $n_0$ of symmetric (homogeneous) nuclear matter (SNM) at equilibrium, the inhomogeneities have been smoothed out and we enter the core of the star. The homogeneous medium of which the core is comprised is known as "neutron-star matter" (N*M), and it is made up primarily of neutrons, with a small admixture of protons neutralized by electrons (and muons at densities above $\bar{n} \simeq 0.12$ fm$^{-3}$). Closer to the center, other particles such as hyperons might appear.

In this paper we continue our calculations of the different regions of neutron stars with a family of three Skyrme-type functionals, BSk19, BSk20, and BSk21, that we have constructed specifically to provide a unified approach not only to the structure of the different regions of neutron stars but also to other phenomena associated with the birth and death of neutron stars, e.g., core-collapse supernovae, the r-process of nucleosynthesis in the neutrino-driven wind, and nucleosynthesis via the decompression of neutron-star matter [3]. These three functionals are all based on effective forces with the generalized Skyrme form

$$\begin{aligned} v_{ij} = {} & t_0(1 + x_0 P_\sigma)\delta(\boldsymbol{r}_{ij}) + \frac{1}{2}t_1(1 + x_1 P_\sigma)\frac{1}{\hbar^2}\left[p_{ij}^2\,\delta(\boldsymbol{r}_{ij}) + \delta(\boldsymbol{r}_{ij})\,p_{ij}^2\right] + t_2(1 + x_2 P_\sigma)\frac{1}{\hbar^2}\boldsymbol{p}_{ij}.\delta(\boldsymbol{r}_{ij})\,\boldsymbol{p}_{ij} \\ & + \frac{1}{6}t_3(1 + x_3 P_\sigma)\,n(\boldsymbol{r})^\alpha\,\delta(\boldsymbol{r}_{ij}) + \frac{1}{2}\,t_4(1 + x_4 P_\sigma)\frac{1}{\hbar^2}\left[p_{ij}^2\,n(\boldsymbol{r})^\beta\,\delta(\boldsymbol{r}_{ij}) + \delta(\boldsymbol{r}_{ij})\,n(\boldsymbol{r})^\beta\,p_{ij}^2\right] \\ & + t_5(1 + x_5 P_\sigma)\frac{1}{\hbar^2}\boldsymbol{p}_{ij}.n(\boldsymbol{r})^\gamma\,\delta(\boldsymbol{r}_{ij})\,\boldsymbol{p}_{ij} + \frac{\mathrm{i}}{\hbar^2}W_0(\boldsymbol{\sigma}_i + \boldsymbol{\sigma}_j)\cdot\boldsymbol{p}_{ij}\times\delta(\boldsymbol{r}_{ij})\,\boldsymbol{p}_{ij}, \end{aligned} \tag{1}$$

where $\boldsymbol{r}_{ij} = \boldsymbol{r}_i - \boldsymbol{r}_j$, $\boldsymbol{r} = (\boldsymbol{r}_i + \boldsymbol{r}_j)/2$, $\boldsymbol{p}_{ij} = -\mathrm{i}\hbar(\boldsymbol{\nabla}_i - \boldsymbol{\nabla}_j)/2$ (the relative momentum), $P_\sigma$ is the two-body spin-exchange operator, and $n(\boldsymbol{r}) = n_n(\boldsymbol{r}) + n_p(\boldsymbol{r})$ is the total local density, $n_n(\boldsymbol{r})$ and $n_p(\boldsymbol{r})$ being the neutron and proton densities, respectively. The $t_4$ and $t_5$ terms here are unconventional, being density-dependent generalizations of the $t_1$ and $t_2$ terms, respectively.

The parameters of this form of force were determined primarily by fitting measured nuclear masses, which were calculated with the Hartree-Fock-Bogoliubov (HFB) method. For this it was necessary to supplement the Skyrme forces with a microscopic contact pairing force, phenomenological Wigner terms and correction terms for the spurious collective energy. However, in fitting the mass data we simultaneously constrained the Skyrme force to fit the zero-temperature equation of state (EOS) of homogeneous neutron matter (NeuM), as determined by many-body calculations with realistic two- and three-nucleon forces; the strength of the

 

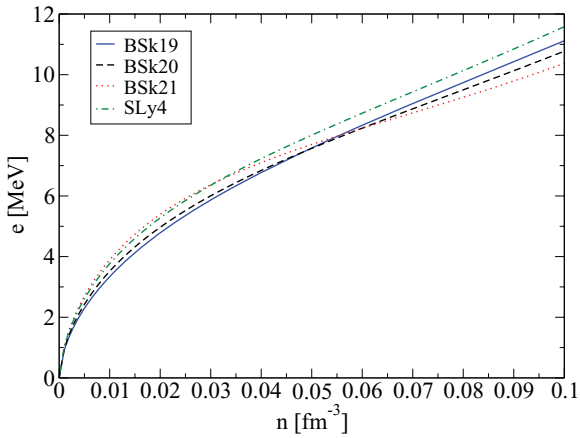


FIG. 1. (Color online) Neutron-matter equations of state (internal energy per nucleon $e$ as a function of density $n$) for forces BSk19–BSk21 and SLy4 at subnuclear densities and zero temperature.

pairing force at each point in the nucleus in question was likewise calculated analytically so as to reproduce the $^1S_0$ pairing gaps of homogeneous nuclear matter of the appropriate density and charge asymmetry [4]. Actually, several realistic calculations of the EOS of NeuM have been made, and while they all agree very closely at nuclear and subnuclear densities, at the much higher densities that can be encountered toward the center of neutron stars they differ greatly in the stiffness, i.e., the density dependence, of the symmetry energy that they predict, and there are very few data, either observational or experimental, to discriminate among the different possibilities. It is in this way that we arrived at the three different functionals of this paper: BSk19 corresponds to the softest EOS of NeuM known to us, BSk21 corresponds to the stiffest, while BSk20 has intermediate symmetry stiffness, as seen in Fig. 1 of Ref. [3]. On the other hand, Fig. 1 of the present paper shows that in NeuM the three functionals are very close to each other at the subnuclear densities relevant to neutron-star crusts. For a further discussion of this point see Ref. [3], where it will be seen in particular that a value of 30 MeV was imposed on the symmetry coefficient $J$ for all three functionals. It will also be seen there that the values of the density-symmetry coefficient $L$, which measures the stiffness of the symmetry energy *at the equilibrium density* $n_0$, are all very similar.

Furthermore, we imposed on these functionals the supplementary constraints of (i) eliminating all unphysical instabilities in nuclear matter for all densities up to the maximum found in neutron stars (these functionals being also stable at the finite temperatures encountered in supernova cores [5]), (ii) obtaining a qualitatively realistic distribution of the potential energy among the four spin-isospin channels in nuclear matter, and (iii) ensuring that the isovector effective mass is smaller than the isoscalar effective mass, as indicated by both experiment and many-body calculations.

The introduction of the unconventional terms in $t_4$ and $t_5$ allowed us to satisfy all these constraints and at the same time fit the 2149 measured masses of nuclei with $N$ and $Z \geqslant 8$ given in the 2003 AME (Atomic Mass Evaluation) [6] with an rms deviation as low as 0.58 MeV for all three models, i.e., for all three options for the high-density variation of the symmetry energy. For all three of these functionals, complete mass tables (labeled HFB-19, HFB-20, and HFB-21, respectively) were constructed, going from one drip line to the other. The reliability of the predictions that these models make for experimentally inaccessible neutron-rich nuclei is all the greater for the constraints to neutron matter imposed on their underlying forces, and it was thus particularly appropriate to use these mass models in our earlier study of the outer crust of neutron stars [7]. For the homogeneous core, the $T = 0$ equations of state of N*M for our forces BSk19, BSk20, and BSk21 have already been published in the original paper presenting these forces [3]. This leaves just the inner crust to be dealt with, and our main concern in this paper is to calculate for this region the EOS and the composition as a function of density with each of our three functionals.

We shall also perform inner-crust calculations with the functional SLy4 [8], since like our own functionals it is designed for finite-nucleus HFB calculations and is intended for neutron-star studies, being subject to a neutron-matter constraint. However, it has the conventional Skyrme form and thus, having fewer parameters, is far less flexible than our own functionals. Thus SLy4 was fitted to only six nuclear masses; moreover, three of these nuclei had $N = Z$ (even), and since no Wigner term was included in the model the symmetry energy must inevitably be too large. (In particular, the symmetry coefficient $J$ for this functional is 32 MeV, while we have found that the optimal value for the conventional form of Skyrme functional when all the mass data are fitted without any neutron-matter or other constraint is 28 MeV [9].) The excessive symmetry energy might explain why the rms deviation from the mass data is quite large, 5.1 MeV [10]; note that only even-even nuclei were considered in that calculation.

Given that all four functionals were fitted to masses with the HFB method, it might seem appropriate to use this method for the inner-crust calculations as well. Now the latter calculations have been generally performed within the framework of the spherical Wigner-Seitz (WS) approximation, as in the pioneering HF calculations of Negele and Vautherin [11], in order to avoid computer times grossly in excess of those for isolated-nucleus calculations. But an inevitable consequence of the WS approximation is the introduction of shell effects in the spectrum of unbound neutron states, which dominate the properties of the inner crust. Such shell effects are to a large extent spurious, since in reality the unbound neutron states form a quasicontinuum. This difficulty is analyzed in detail in Refs. [12,13], the latter reference showing that the error thereby introduced in the energy per nucleon cannot easily be reduced below 50 keV, which is incompatible with a reliable calculation of the composition of the inner crust; for a very recent discussion of the problem see Grill *et al.* [14]. In the last few years three-dimensional calculations have been carried out by several groups [15–17]. However, not only does this sort of calculation require computer times that are quite impractical for extensive astrophysical calculations but the use of a cubic box with periodic boundary conditions can still lead to spurious neutron shell effects (see, for example, Sec. C.2 in Ref. [17]).

In view of these problems it is not surprising that a more popular approach to the calculation of the inner crust has

been to use the much simpler compressible liquid-drop model (CLDM); a typical such calculation is that of Ref. [18]. Within each Wigner-Seitz cell this method makes a clear separation of nuclear matter into two distinct homogeneous phases, the densities of which are free parameters of the model. The bulk properties of the two phases are calculated microscopically using the adopted functional, as are the surface properties (preferably including curvature corrections) of the interface between them. A more realistic treatment of spatial inhomogeneities is to employ semiclassical methods such as the Thomas-Fermi (TF) approximation, as for instance in Ref. [19]. However, both the CLDM and TF methods are otherwise purely macroscopic, and in particular they have no quantum shell corrections at all.

The so-called temperature-dependent extended Thomas-Fermi plus Strutinsky integral (TETFSI) method of Onsi *et al*. [20], which we adopt here, is a computationally very fast approximation to the full finite-temperature HF method. This method was originally developed for calculating the EOS of the dense matter found in supernova cores [21]. But in this work we will be using just the zero-temperature limit. The TETFSI method, like the TF method, allows for a continuous variation of the density of nuclear matter within each WS cell, without any artificial separation into two distinct phases. However, it is expected to provide a much better description of nuclear clusters than the TF method because the semiclassical expressions for the kinetic-energy and spin current densities include density-gradient terms up to the fourth order. Most importantly, proton shell corrections are added perturbatively, but we avoid the difficulty of spuriously large values for the neutron shell corrections noted above by not calculating them at all; in any case they are known to be much smaller than the proton shell corrections [13,22,23].

Our method is described in detail in Ref. [20], but we summarize it here in Sec. II. The results for the zero-temperature composition and EOS of the inner crust are presented in Sec. III, along with an examination of the extent to which continuity holds at the interface with the outer crust. This section also discusses the transition between the inner crust and the liquid core. In Sec. IV we examine the solutions to the Tolman-Oppenheimer-Volkoff (TOV) equations [24,25] in order to determine the distribution of mass within the inner crust. Our conclusions are summarized in Sec. V.

## II. TETFSI MODEL OF THE INNER CRUST

To summarize the main features of the TETFSI method [20], we note first that it models the inhomogeneous medium by spherical WS cells, with the spherically symmetric neutron and proton density distributions being parametrized according to

$$n_q(r) = n_{Bq} + n_{\Lambda q} f_q(r), \tag{2}$$

in which, with $q = n$ or $p$, $n_{Bq}$ is a constant background term, while

$$f_q(r) = \frac{1}{1 + \exp\left\{\left(\frac{C_q - R}{r - R}\right)^2 - 1\right\} \exp\left(\frac{r - C_q}{a_q}\right)}. \tag{3}$$

In this "damped" form of the usual simple Fermi profile all density derivatives vanish at the surface of the cell, thereby ensuring a smooth matching of the nucleonic distributions between adjacent cells and satisfying certain necessary conditions discussed below. It is particularly to be noted that with this parametrization of the density there is no arbitrary separation into liquid and gaseous phases within the WS cell. However, if this were what is energetically favored in reality, it would automatically be taken into account through the small values of the diffusenesses $a_q$ that would emerge.

In order to determine the composition and the EOS of the inner crust one should in principle minimize at constant pressure the Gibbs free energy $g$ per nucleon with respect to all the parameters of the WS cell. This is the procedure that we adopted in Ref. [7] for the outer crust, but for the inner crust the computation would be extremely heavy. Instead, we minimize rather the total Helmholtz free energy $f$ per nucleon at constant mean density $\bar{n}$ with respect to the same parameters, showing in Appendix A that the error thereby introduced is quite negligible. Since the present work is limited to $T = 0$ it is the internal energy per nucleon, $e$, that is minimized ($f = e - Ts$, where $s$ is the entropy per nucleon).

To enumerate the minimizing parameters of the WS cell, we note first that the cell radius $R$ will be determined, for the given $\bar{n}$, by the total number $A$ of nucleons in the cell. Then with the number of protons, $Z$, and the number of neutrons, $N$, in the cell specified ($Z + N = A$), only three of the four remaining cell parameters appearing in Eqs. (2) and (3) for each charge type of nucleon will be independent. Thus, including $Z$ and $N$, there will be eight parameters with respect to which the energy $e$ must be minimized. Identifying the different contributions to $e$, we write

$$e = e_{\rm nuc} + e_e + e_c - Y_e\, Q_{n,\beta}, \tag{4}$$

and now discuss briefly each term.

The nuclear term is

$$e_{\rm nuc} = \frac{4\pi}{A} \int_{\rm cell} r^2 \mathcal{E}^{\rm ETF}_{\rm Sky}(r) dr + e^p_{\rm sh}, \tag{5}$$

where $\mathcal{E}^{\rm ETF}_{\rm Sky}(r)$ is the extended Thomas-Fermi (ETF) approximation to the energy density $\mathcal{E}_{\rm Sky}(r)$ given by Eq. (A3) of Ref. [26] for the generalized Skyrme force (1). (The formalism of Ref. [20] is limited to conventional Skyrme forces.) All terms in $\mathcal{E}_{\rm Sky}$ are functions of the number densities $n_q(r)$, the kinetic-energy densities $\tau_q(r)$, and the spin-current densities $\boldsymbol{J}_q(r)$. The ETF method approximates these last two densities as functions of the number densities $n_q(r)$ and their first four derivatives. However, as far as the total ETF energy is concerned, it is shown in Appendix A of Brack *et al*. [27] that the third- and fourth-order derivatives of the density can be eliminated by partial integration over the region of interaction, provided certain boundary conditions are satisfied on the bounding surface of this region. In the finite-nucleus case of Ref. [27] the bounding surface can be taken to lie at infinity, in which case the necessary boundary conditions are trivially easy to satisfy. In the present case the bounding surface is the surface of the WS cell, and, given the fact that in general the density does not vanish on this surface, the necessary conditions are that the first three derivatives of the density

must vanish there. These conditions are satisfied automatically for the distribution (3), and it is in this "integrated" form that we have implemented the ETF method. Note that for all four functionals, i.e., BSk19–BSk21 and SLy4, we omit the spin-current terms in $J^2$, since this is the way these functionals were fitted (see Ref. [5] for a discussion of the implications of these terms for spin and isospin stability).

With the ETF approximations for $\tau_q(r)$ and $\boldsymbol{J}_q(r)$ being semiclassical all shell effects in $\mathcal{E}_{\rm Sky}(r)$ are lost. The second term on the right-hand side of Eq. (5) represents our attempt to restore the proton shell corrections perturbatively using the Strutinsky integral (SI) method, as described in Ref. [20]. As explained in Sec. I, we do not calculate neutron shell corrections in the inner crust; for a fuller discussion of this point see Sec. I of Ref. [20], where we conclude that, because of the problems with neutrons, the ETFSI method is better adapted to a WS approach than is the HFB (or HF-BCS) method. On the other hand, we do not include pairing at the present stage of our calculations. This should have very little impact on the EOS, but it might have implications for the composition.

The term $e_e$ on the right-hand side of Eq. (4) denotes the kinetic energy per nucleon of the electrons. In dense, cold neutron star crust, electron-charge screening effects are negligible and the electron density $n_e = \bar{n}_p$ is essentially uniform [28,29]. The energy $e_e$ can thus be calculated straightforwardly by expressions given in Sec. 24 of Cox and Giuli [30], as in Ref. [20].

The third term on the right-hand side of Eq. (4) denotes the total Coulomb energy per nucleon. It is calculated according to Eq. (3.4) of Ref. [20], except that there are the following changes to the exchange part. (a) The proton exchange energy is set equal to zero for the three BSk functionals; this is a device that we have successfully adopted in all our recent models, beginning with BSk15 [31], and it can be interpreted as compensating for neglected effects such as Coulomb correlations, charge-symmetry breaking of the nuclear forces, and vacuum polarization. (b) The electron exchange energy, which has the nonrelativistic form in Eq. (3.4) of Ref. [20], is multiplied by a factor of $-1/2$, as appropriate for extremely relativistic particles [32].

The last term on the right-hand side of Eq. (4), in which $Q_{n,\beta}$ is the $\beta$-decay energy of the neutron (0.782 MeV) and $Y_e = Z/A$, takes account of the neutron-proton mass difference (where we drop a constant term $M_n c^2$).

Minimization of $e$ with respect to the eight available parameters is performed by means of the CERN routine MINUIT. Actually, we found it necessary to exclude the shell correction term $e^p_{\rm sh}$ from this minimization, and then to add it later to what is really just the optimal ETF part of the energy. Otherwise, the minimization routine will tend to seek large negative values of the shell corrections, in violation of the essentially perturbative character of the SI method. In practice, we performed the minimization for different fixed values of $Z$, thereby reducing the number of free variational parameters to seven. However, even with this reduced number of parameters MINUIT occasionally failed to find a correctly converged minimum. This problem could often, but not always, be avoided by adjusting the initial values for the parameters. When this procedure failed, solutions could always be found, provided we are not too close to the interface with the core, by a slight shift in the value of $\bar{n}$; for this reason our grid of values of $\bar{n}$ is irregular. However, above a certain value of $\bar{n}$ we were unable to find any solutions at all when MINUIT minimizes with respect to seven variables. We attribute the failure of our code to find well-defined minima before true homogeneity has been reached to the energy minimum being very flat, with the result that MINUIT is unable to pick out one configuration among a very wide range of possibilities. We found, however, that we could still find well-defined minima in this region by reducing the number of free variables in MINUIT to three, $n_{\Lambda n}$, $n_{\Lambda p}$, and $N$, and minimizing for a large number of fixed values of the other five parameters; clearly, for a given level of accuracy this procedure will require much more computation time than when MINUIT minimizes on seven variables.

It should be noted that at all densities the number of neutrons, $N$, in the WS cell is taken as one of the minimizing variables in MINUIT and hence is treated as a continuous variable, rather than being discretized to integral values. Even though the total number of neutrons in the crustal layer is, of course, integral, the notion of a fractional number of neutrons per WS cell corresponds, in fact, to the physical reality, since the neutrons are delocalized.

Normally, we would expect positive values of the constants $n_{\Lambda n}$ and $n_{\Lambda p}$ to emerge from the minimization, the cluster then representing a "droplet." However, there have been indications [1,2] that toward the interface with the core the clusters may take several other forms. Most of these "pasta" configurations, such as slabs, tubes, and rods, cannot be handled by our code, which is restricted to spherical shapes, but another of these possibilities, spherical bubbles, could in principle emerge from the minimization with our code, since they correspond simply to negative values of $n_{\Lambda q}$. We return to this possibility in Sec. III C.

The pressure $P$ corresponding to any given value of $\bar{n}$ is calculated by evaluating a simple analytic expression, as described in Appendix B. This is more reliable and computationally much faster than the numerical differentiation of $e$ used in Ref. [20].

## III. COMPOSITION AND EQUATION OF STATE OF THE INNER CRUST

### A. Generalities

Following the methods described in the previous section, for each of our three functionals and SLy4 we minimized the internal energy per nucleon, $e$, at temperature $T = 0$ for more than a hundred different densities $\bar{n}$ between the drip point and 0.1 fm$^{-3}$. At this upper limit our density distributions have become effectively homogeneous, as will be discussed in more detail in Sec. III C.

For all values of $\bar{n}$ up to 0.06 fm$^{-3}$ the optimal value of the number of protons, $Z$, per Wigner-Seitz cell was found to be 40, for all four functionals. However, at higher densities, as homogeneity is approached, the minimized energy becomes increasingly insensitive to $Z$. The preference for $Z = 40$ in the case of these four functionals is somewhat fortuitous,

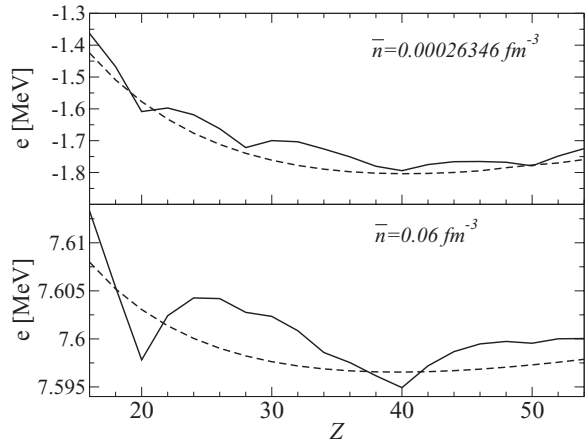


FIG. 2. Variation of ETFSI energy $e$ per nucleon as a function of $Z$ for functional BSk19 with $N$ optimized for each value of $Z$; the dotted curve represents the ETF approximation. Upper panel: $\bar{n} = 2.63 \times 10^{-4}$ nucleons fm$^{-3}$ (drip density); lower panel: $\bar{n} = 0.06$ nucleons fm$^{-3}$.

given that for some of our older functionals different values were found. For example, with the functional BSk14 used in Ref. [20] it was found that $Z$ could take any of the values, 20, 40 and 50, according to the density. It is remarkable that these familiar finite-nucleus magic proton numbers should persist in the highly neutron-rich environment beyond the drip line, especially in view of the presence of electrons, which will have the effect of significantly reducing Coulomb effects.

For the specific case of functional BSk19, reference to Fig. 2 shows both the role of shell effects and the overall trends imposed by the ETF part of the calculation. For both of the extreme densities shown here the ETF minimum lies close to $Z = 40$, and the shell effects simply reinforce this preference. However, the energy difference per nucleon, $\Delta e$, between $Z = 40$ and $Z = 50$ is very small: about 10 keV at the drip density and 5 keV at $\bar{n} = 0.06$ fm$^{-3}$ (and note the different energy scales of the two panels). It is easy to see how with even an only very slightly different functional a quite different $T = 0$ composition could be found, as a result of changes in either the shell effects or the macroscopic ETF part of the energy (or both).

Since the functionals BSk19, BSk20, and BSk21 give better and wider data fits than all our earlier functionals, and have a better theoretical base as well, we believe our prediction of $Z = 40$ at all densities in the inner crust to be more credible than our earlier predictions, but the need for caution is evident. For example, taking pairing into account might well shift the favored value of $Z$ away from 40. In any case, in a real neutron star a fairly wide range of values of $Z$ can be expected at any point in the inner crust because of the finite temperature.

The optimal values of $A$ are plotted as a function of the density in Fig. 3; similarly, Figs. 4 and 5 show the variation of $e$ and the pressure $P$, respectively; these two figures show the densities $\bar{n}_{\rm trans}^{N*M}$ of transition between the inner crust and the core, as calculated in Sec. III C.

No essential differences will be perceived among any of these four functionals, as far as the inner crust is concerned,

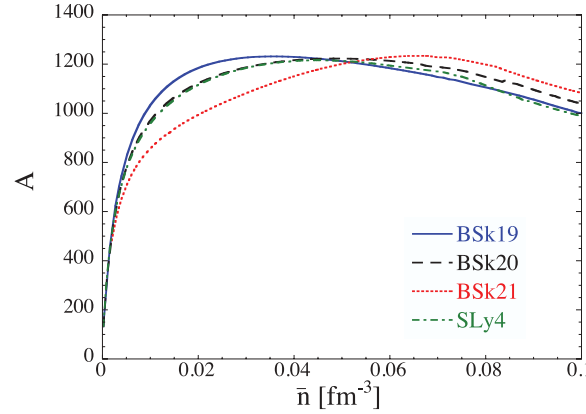


FIG. 3. (Color online) Optimal value of nucleon number $A$ as a function of density $\bar{n}$ at zero temperature in the inner crust; the proton number $Z$ everywhere takes an optimal value of 40 for all four forces.

although BSk21 is seen in Fig. 5 to have a somewhat softer EOS (in contrast to a much stiffer EOS at high density). These features can be related to the behavior of the respective functionals in homogeneous NeuM at inner-crust densities (see Fig. 1). Since SLy4 gives a much worse mass fit than do any of the BSk functionals, one might have expected that it would represent less well the presence of inhomogeneities and of protons, and thus give significantly different results in the inner crust, but this turns out not to be the case. Furthermore, the higher value of the symmetry coefficient $J$ in the case of SLy4 (32 MeV, as opposed to 30 MeV in the case of all the BSk functionals) does not seem to have much impact.

### B. Continuity with the outer crust

Our inner-crust code, as used here, is in principle applicable to the outer crust, with the background densities $n_{Bq}$ vanishing automatically on minimizing the energy per nucleon, and it is thus meaningful to compare this code with the code we used for the outer-crust calculation of Ref. [7]. In Table I we make this comparison at the drip-point density $\bar{n}_{\rm drip}$ (as determined by

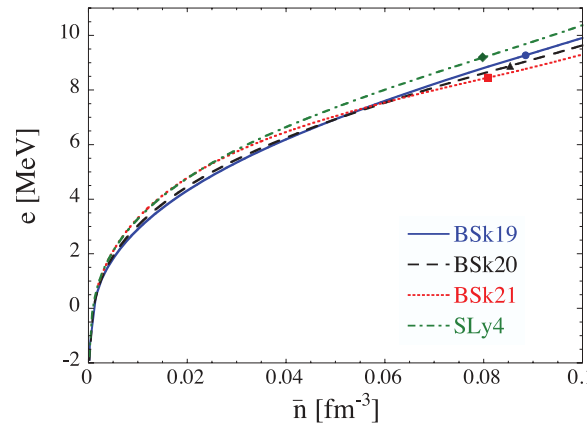


FIG. 4. (Color online) Internal energy $e$ per nucleon at zero temperature as a function of density $\bar{n}$ in the inner crust. The solid symbols represent the transition densities $n_{\rm trans}^{N*M}$ (see Sec. III C).

TABLE I. Comparison of inner-crust and outer-crust codes at the drip point; results for the latter code are in parentheses. $e$ is the internal energy per nucleon, and $P$ is the pressure.

| Force | $\bar{n}_{\rm drip}$ (fm$^{-3}$) | $Z$ | $N$ | $e$ (MeV) | $P$ (MeV fm$^{-3}$) |
|---|---|---|---|---|---|
| BSk19 | $2.63464 \times 10^{-4}$ | 40 (38) | 96 (88) | −1.79426 (−1.87464) | $5.072 \times 10^{-4}$ ($4.938 \times 10^{-4}$) |
| BSk20 | $2.62873 \times 10^{-4}$ | 40 (38) | 95 (88) | −1.79451 (−1.87305) | $5.064 \times 10^{-4}$ ($4.923 \times 10^{-4}$) |
| BSK21 | $2.57541 \times 10^{-4}$ | 40 (38) | 94 (86) | −1.81718 (−1.90057) | $4.984 \times 10^{-4}$ ($4.894 \times 10^{-4}$) |
| SLy4 | $2.45897 \times 10^{-4}$ | 40 (38) | 93 (82) | −1.78801 (−1.95898) | $4.744 \times 10^{-4}$ ($4.807 \times 10^{-4}$) |

the code for the outer crust) with the results for the outer-crust code shown in parentheses.

We see that the inner-crust code (TETFSI) underbinds with respect to the outer-crust code (HFB) by around 5%. This disagreement can be accounted for by the several approximations made in our TETFSI method, relative to the HFB method adopted in our outer-crust calculations [7], as follows. (i) The kinetic energy and spin currents are calculated with the semiclassical (T)ETF method. (ii) Proton shell corrections are put in perturbatively, and neutron shell corrections (shown in Refs. [13,23] to be much smaller than proton shell corrections as soon as neutron drip sets in, but obviously not zero in the outer crust) are neglected completely. (iii) Rather than allowing arbitrary density variations when minimizing the total energy, the density is parametrized according to Eqs. (2) and (3). (iv) Pairing is neglected completely. We have checked that the assumption of sphericity in the inner-crust code has a negligible impact in this region of the nuclear chart.

It will also be seen from Table I that there is a slight disagreement in the values of $Z$ and $N$ at the drip point. One might speculate that the favoring of $Z = 40$ over 38 is the result of an exaggerated shell effect, but if we drop the proton shell corrections altogether then we find slightly higher values of $Z$, typically 41. However, we have already remarked how the inclusion of pairing might well shift the unique value of $Z$ (at $T = 0$) away from 40, and we see from Fig. 2 that *a priori* it would be difficult to rule out any value of $Z$ between 36 and 50 at the drip density. The disagreement in the neutron number $N$ is somewhat larger, presumably because of our neglect of neutron shell effects, but it is $Z$ that is the more astrophysically relevant nucleonic number.

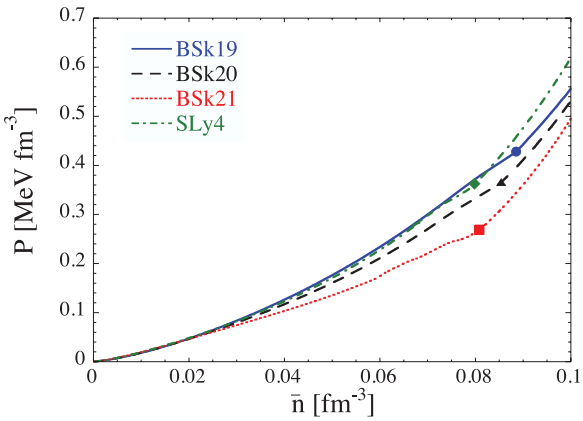


FIG. 5. (Color online) Pressure $P$ per nucleon at zero temperature as a function of density $\bar{n}$ in the inner crust. The solid symbols represent the transition densities $n_{\rm trans}^{N*M}$ (see Sec. III C).

### C. Transition to the homogeneous core

The densities $n_{\rm trans}^{N*M}$ shown in Figs. 4 and 5 and tabulated in Table II are the densities below which homogeneous $\beta$-equilibrated N*M is calculated, for the functional in question, to be unstable to breakup into inhomogeneities. Our values for $n_{\rm trans}^{N*M}$ were calculated by the method described in Ref. [33], in which one defines a free-energy curvature matrix by

$$C_{\rm NMe,dyn} = \begin{pmatrix} \frac{\partial \mu_n}{\partial n_n} & \frac{\partial \mu_n}{\partial n_p} & 0 \\ \frac{\partial \mu_p}{\partial n_n} & \frac{\partial \mu_p}{\partial n_p} & 0 \\ 0 & 0 & \frac{\partial \mu_e}{\partial n_e} \end{pmatrix} + k^2 \begin{pmatrix} 2C_{nn}^{\nabla} & 2C_{np}^{\nabla} & 0 \\ 2C_{pn}^{\nabla} & 2C_{pp}^{\nabla} & 0 \\ 0 & 0 & 0 \end{pmatrix} + \frac{4\pi^2 e^2}{k^2} \begin{pmatrix} 0 & 0 & 0 \\ 0 & 1 & -1 \\ 0 & -1 & 1 \end{pmatrix}, \quad (6)$$

where the $\mu_i (\equiv \frac{\partial f}{\partial n_i})$ are the neutron, proton, and electron chemical potentials; note that $n_e = \bar{n}_p$. The coefficients $C_{ij}^{\nabla}$ account for the density-gradient terms in the nuclear density functional, which come into play in the presence of inhomogeneities. The third term on the right-hand side of this equation gives the Coulomb contribution. Stability of N*M against breakup (actually, against density fluctuations of infinitesimally small amplitude) will be assured as long as the curvature matrix $C_{\rm NMe,dyn}$ has no negative eigenvalues for all real values of $k$, the wave number of density fluctuations. Thus in practice one calculates the lowest eigenvalue of $C_{\rm NMe,dyn}$ along the line of $\beta$ equilibrium of N*M in the $n_n$-$n_p$ plane and determines the density $n_{\rm trans}^{N*M}$ at which it changes sign. Along with $n_{\rm trans}^{N*M}$, Table II also shows the value of the proton fraction $Y_e$ and the pressure at the transition point.

It is instructive to see how our density distributions, as given by Eq. (2), approach homogeneity as the density increases. In Fig. 6 we follow the approach to homogeneity by showing the neutron and proton density profiles within the WS cell

TABLE II. Parameters relating to the crust-core transition.

| Force | $n_{\rm trans}^{N*M}$ (fm$^{-3}$) | $Y_e$ | $P_{\rm trans}$ (MeV fm$^{-3}$) |
|---|---|---|---|
| BSk19 | 0.0885 | 0.0376 | 0.428 |
| BSk20 | 0.0854 | 0.0356 | 0.365 |
| BSk21 | 0.0809 | 0.0335 | 0.268 |
| SLy4 | 0.0798 | 0.0358 | 0.361 |

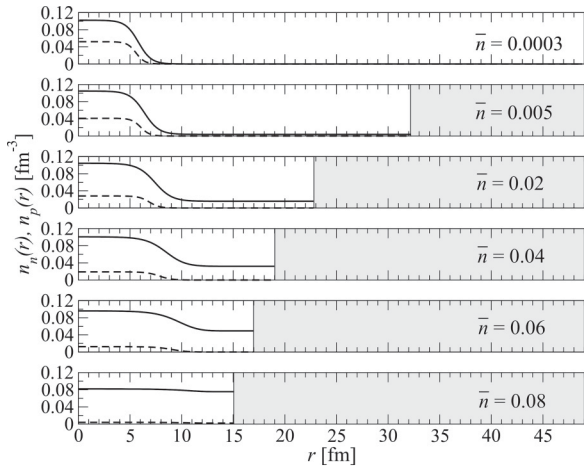


FIG. 6. Profiles of neutron (solid curves) and proton (dashed curves) density distributions in the Wigner-Seitz cell for functional BSk21 and different values of the mean density $\bar{n}$. Shading denotes the region beyond the cell radius.

for different values of the mean density $\bar{n}$. As far as can be seen from this figure, the transition to homogeneous matter is very smooth, with no evidence of any discontinuity. However, it is not clear in this figure at what precise density homogeneity can be said to set in, but Figs. 7 and 8 complete the picture in this respect. The former shows the variation of the "cluster strength" parameters $n_{\Lambda n}$ and $n_{\Lambda p}$ as a function

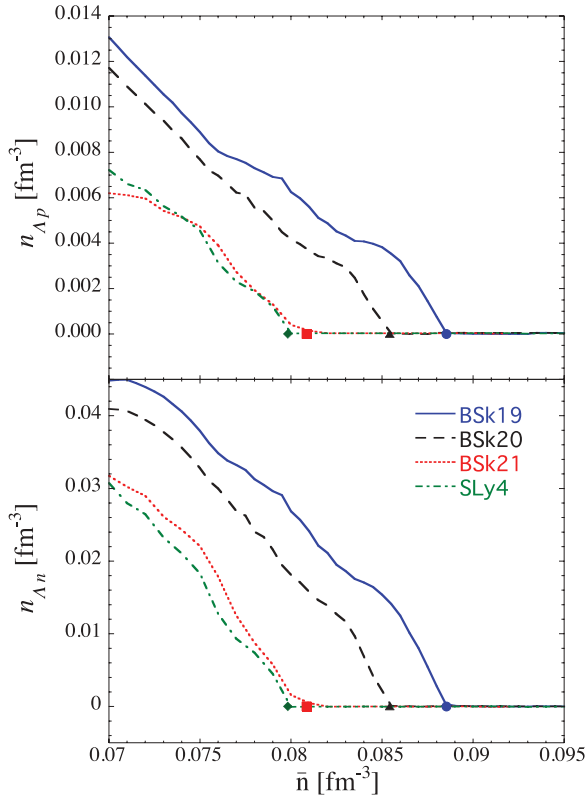


FIG. 7. (Color online) Variation of the "cluster strength" parameters $n_{\Lambda n}$ and $n_{\Lambda p}$ as a function of density [see Eq. (2)]. The solid symbols represent the transition densities $n_{\rm trans}^{N*M}$ (see Sec. III C).

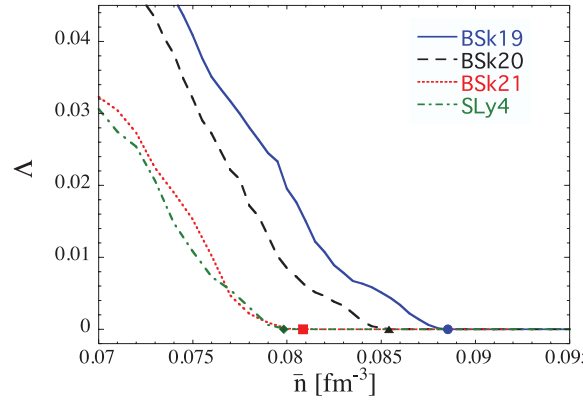


FIG. 8. (Color online) Variation of the inhomogeneity factor $\Lambda$, given by Eq. (7), as a function of density. The solid symbols represent the transition densities $n_{\rm trans}^{N*M}$ (see Sec. III C).

of density: Eq. (2) shows that homogeneity corresponds to these parameters being equal to zero. Now in Fig. 7 we see that, for all functionals, these parameters vanish when the density is very close to $n_{\rm trans}^{N*M}$, calculated as described above by a completely different method. A similar conclusion can be drawn from Fig. 8, where we plot a more global measure of the departure from homogeneity, the "inhomogeneity factor"

$$\Lambda = \frac{1}{V_{\rm cell}} \int d^3\mathbf{r} \left( \frac{n(\mathbf{r})}{\bar{n}} - 1 \right)^2 , \qquad (7)$$

where $V_{\rm cell}$ is the volume of the WS cell and the integration goes over the cell. We plot this as a function of density in Fig. 8, where the transition to homogeneity at a density very close to the density $n_{\rm trans}^{N*M}$ is again apparent.

We stress also that in both Figs. 7 and 8 the fall to zero of the appropriate measure of inhomogeneity is smooth, with no indication of any discontinuity. We cannot exclude the possibility that the transition is first order, albeit very weak, but all our results are consistent with the transition being of second order or higher.

Figures 6 and 7 make it clear that for none of the four functionals considered here have we found a spherical bubble configuration anywhere in the inner crust. That is, energy minimization always leads to a droplet configuration until homogeneity is reached. This result confirms, as far as force SLy4 is concerned, the CLDM calculations of Douchin and Haensel [34]. However, we cannot exclude the possibility of very shallow bubbles in a very narrow density range, although such configurations would be of limited astrophysical interest. Note, moreover, that since our calculations are limited to spherical configurations we can say nothing about nonspherical bubbles, such as the very shallow ones found for SLy4 in Ref. [16].

## IV. DISTRIBUTION OF MASS

With the EOS determined (for a given functional), the distribution of mass within a neutron star (assumed to be nonrotating) is given by the solution to the TOV

equations [24,25],

$$\frac{dP(r)}{dr} = -\frac{G\rho(r)\mathcal{M}(r)}{r^2}\left[1+\frac{P(r)}{c^2\rho(r)}\right]\left[1+\frac{4\pi P(r)r^3}{c^2\mathcal{M}(r)}\right] \times\left[1-\frac{2G\mathcal{M}(r)}{c^2 r}\right]^{-1} \quad (8)$$

and

$$\mathcal{M}(r) = 4\pi\int_0^r \rho(r')r'^2 dr'. \quad (9)$$

Here $\rho(r)$ is the mass-energy density at the radial coordinate $r$, given by

$$\rho(r) = \bar{n}(r)\left(M+\frac{e}{c^2}\right), \quad (10)$$

where $M$ is the nucleon mass and $e$ is the internal energy per nucleon, as plotted in Fig. 4. The pressure $P(r)$ appearing in Eq. (8) has to be expressed in terms of $\rho(r)$ through the EOS.

Proceeding as in Sec. III C of Ref. [7], we solve the TOV equations (8) and (9) for the functions $\rho(r)$ and $\mathcal{M}(r)$ by integrating inward from the surface. (If we had followed the usual procedure of integrating outward from the center our crust results would have been contaminated by the uncertainties in the EOS of the core.) Then the total baryonic mass of the shell of inner radius $r$ and outer radius $R$, the radius of the star, is

$$\Delta M_B(r) = 4\pi\, M\int_r^R r'^2\Phi(r')^{1/2}n(r')dr', \quad (11)$$

where we have introduced the metric function

$$\Phi(r) = \left(1-\frac{2G\mathcal{M}(r)}{c^2 r}\right)^{-1}. \quad (12)$$

Note that $\Delta M_B(r)$, as defined by Eq. (11), contains the baryonic mass of the entire outer crust, as calculated in Ref. [7] for the three BSk forces and from Refs. [35,36] for SLy4.

We plot $\Delta M_B(\bar{n}(r))$ as a function of the density $\bar{n}$ in Fig. 9 for a neutron star of mass $1.5M_\odot$ and radius 13 km; the fraction of this mass that consists of protons can be read off from Fig. 3, given that everywhere we have $Z = 40$.

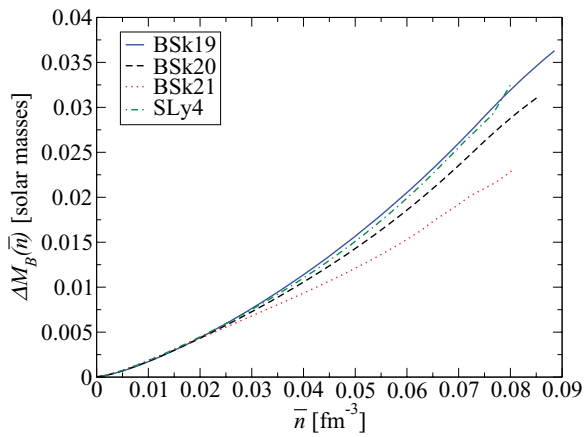


FIG. 9. (Color online) Variation of the baryonic mass of the crust (inner plus outer) with density $\bar{n}$ for a neutron star of mass $1.5M_\odot$ and radius 13 km.

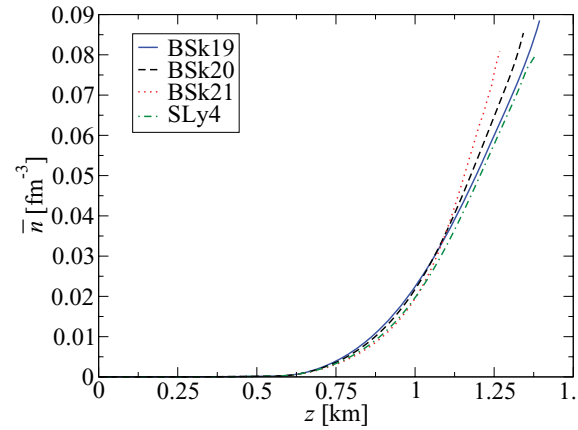


FIG. 10. (Color online) Variation of density $\bar{n}$ with proper depth $z$ for a neutron star of mass $1.5M_\odot$ and radius 13 km.

For many purposes it might be more convenient to express $\Delta M_B$ as a function of the proper depth, given by (see Sec. 5.6 of Ref. [37])

$$z(r) = \int_r^R dr'\left(1-\frac{2G\mathcal{M}(r')}{c^2 r'}\right)^{-1/2}, \quad (13)$$

which is the only measurable depth in the gravitationally distorted metric. We plot in Fig. 10 $\bar{n}$ as a function of $z$, again for a neutron star of mass $1.5M_\odot$ and radius 13 km, whence $\Delta M_B(r)$ can be read off from Fig. 9 as a function of $z$.

In Fig. 11 we show how the total gravitational mass of the crust (inner plus outer) varies as a function of the total star mass for a given radius of 9 km. Figure 12 shows the same function for stars with a radius of 14 km.

## V. CONCLUSIONS

We have calculated the composition and EOS of the inner crust of neutron stars for the three generalized Skyrme-type

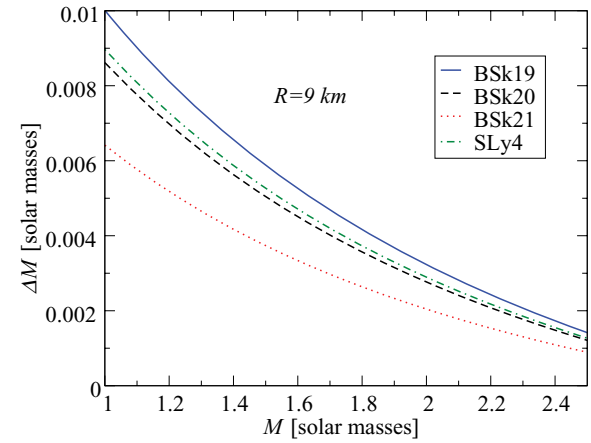


FIG. 11. (Color online) Variation of the gravitational mass of the crust (inner plus outer) with the total mass of a star with a radius of 9 km.

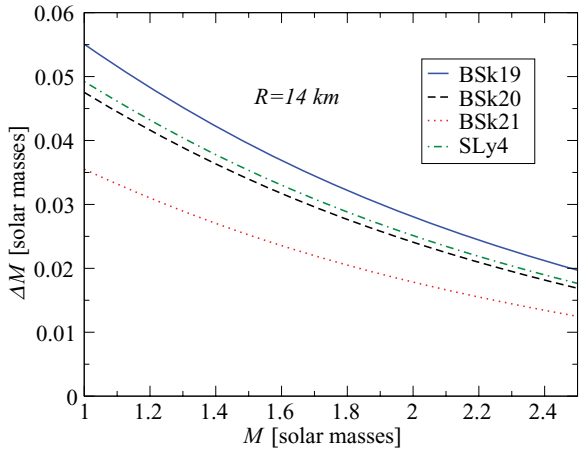


FIG. 12. (Color online) Variation of the gravitational mass of the crust (inner plus outer) with the total mass of a star with a radius of 14 km.

functionals, BSk19, BSk20, and BSk21, and for the conventional Skyrme functional SLy4, using in all cases the TETFSI method at temperature $T = 0$. We have also solved the TOV equations to calculate the distribution of mass within the crust.

Qualitatively similar results are obtained for all four forces. In particular, in all cases we find $Z = 40$ for the optimal number of protons per Wigner-Seitz cell throughout the inner crust. However, other values of $Z$ lie very close in energy, and if we took pairing into account the optimal value of $Z$ might very well be shifted away from 40. Moreover, it is clear that at realistic values of the temperature an appreciable range of values of $Z$ will be found. This underlines the importance of extending the present calculations to finite temperatures and to include pairing.

The fact that there are no substantial differences in the inner-crust properties for force SLy4 and for the three BSk forces despite their having been fitted to different values of the symmetry coefficient $J$ means that this parameter is not of any great relevance in this respect.

We have studied in some detail the transition between the inner crust and the homogeneous core, considering two different measures of the inhomogeneity of our density distributions. We find for each of the four functionals that homogeneity is established in our calculated distributions at a density very close to the value predicted for the onset in homogeneous N*M of instability against density fluctuations of infinitesimally small amplitude.

No evidence for bubbles was found in the course of this study of the transition region, despite a thorough search. This conclusion does not preclude the existence of nonspherical pasta configurations, a possibility that lies beyond the scope of the present paper. Even though such phases would have a negligible impact on the EOS, they might affect transport properties.

The calculations on the inner crust presented here show that our forces BSk19, BSk20, and BSk21 make possible a unified and realistic treatment of all regions of neutron stars, as in Ref. [39].


## ACKNOWLEDGMENTS

We wish to thank M. Brack for helpful comments. This work was financially supported by the NSERC (Canada), the FNRS (Belgium), the Communauté française de Belgique (Actions de Recherche Concertées), and CompStar (a Research Networking Programme of the European Science Foundation).


## APPENDIX A: MINIMIZATION OF GIBBS OR HELMHOLTZ FUNCTIONS?

For simple systems, which in the present context means systems with a single $(N, Z)$ configuration, minimizing the Gibbs free energy per nucleon, $g$, at constant pressure $P$ is completely equivalent to minimizing the Helmholtz free energy per nucleon, $f$, at constant density $\bar{n}$, since in that case the thermodynamic identity

$$\left(\frac{\partial g}{\partial X}\right)_{P,T} = \left(\frac{\partial f}{\partial X}\right)_{\bar{n},T} \tag{A1}$$

holds, where $X$ denotes any thermodynamical variable. But when two different phases or components, i.e., two different $(N, Z)$ configurations in the present context, coexist in equilibrium this identity breaks down, and it is the Gibbs prescription that leads to a correct description of the phase transition: there is a discontinuity in the range of densities over which single-phase solutions can be found, but the pressure remains constant over this discontinuity, which corresponds to the equilibrium coexistence of the two phases. If, on the other hand, one minimizes $f$ at constant density $\bar{n}$, discontinuities in the pressure will be found in the vicinity of transitions from one $(N, Z)$ configuration to another. An example of this is seen in Fig. 13, where we show the transition from $Z = 40$ to $Z = 20$ for functional BSk14 [20], with $N$ being optimized in each case.

Such discontinuities in the pressure are unphysical, and they arise in our calculations only because our model does not allow the coexistence of two different $(N, Z)$ configurations that can

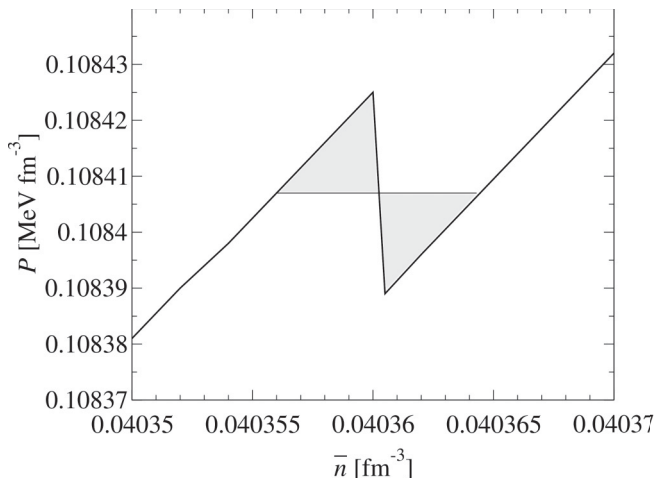


FIG. 13. EOS for functional BSk14 in the vicinity of the $Z = 40$ to $Z = 20$ transition.

occur in reality. But even then, when minimizing $f$ at constant density $\bar{n}$, the correct equilibrium pressure can be found by making a Maxwell construction, as indicated in Fig. 13. However, on the pressure scale of Fig. 5 these discontinuities will be imperceptible, and the Maxwell construction is quite unnecessary: the attendant error will be far smaller than the differences between the equations of state of the different functionals seen in Fig. 5.

In any case, the question of transitions between different values of $Z$ does not arise with functionals BSk19–BSk21, since for all these forces $Z$ retains the constant value of 40 throughout the inner crust. As for changes in $N$, we recall that this varies continuously in our calculations, whence it follows that minimizing $f$ at constant density $\bar{n}$ leads to absolutely no error at all in this respect.

## APPENDIX B: PRESSURE FORMULA

The pressure $P$ at any given point in the neutron-star crust, as given by the EOS and as used in the TOV equations, is defined thermodynamically by considering a region of volume $V$ that contains the point in question and is macroscopically sized but small enough for all intensive thermodynamic variables to be sensibly constant over it. If $F$ denotes the total Helmholtz free energy contained in this region then

$$P = -\left(\frac{\partial F}{\partial V}\right)_{T,N_e,N_q}, \tag{B1}$$

where $T$ is the temperature (here $T = 0$), $N_e$ its number of electrons, and $N_q$ its number of nucleons of type $q = n, p$ for neutrons and protons, respectively. By treating the crust as a perfect crystal, this expression remains exact if the region of volume $V$ is taken as the appropriate Wigner-Seitz cell, because of the translational symmetry. In the approximation used here of spherical WS cells we then have

$$P = -\frac{1}{4\pi R^2}\left(\frac{\partial F}{\partial R}\right)_{T,N_e,N_q}, \tag{B2}$$

where $R$ is the cell radius. We assume that the Helmholtz free energy in the cell can be written as

$$F = 4\pi \int_0^R dr\, r^2 \mathcal{F}(r), \tag{B3}$$

where $\mathcal{F}(r)$ is a functional of the nucleon density $n_q(r)$ and of the electron density $n_e(r)$. These densities are related to the total numbers of nucleons and electrons in the cell by

$$N_q = 4\pi \int_0^R dr\, r^2 n_q(r), \tag{B4a}$$

$$N_e = 4\pi \int_0^R dr\, r^2 n_e(r). \tag{B4b}$$

Combining Eqs. (B2) and (B3) yields

$$P = -\mathcal{F}(R) - \frac{1}{R^2}\int_0^R dr\, r^2 \left(\sum_q \frac{\delta F}{\delta n_q(r)}\frac{\partial n_q(r)}{\partial R} + \frac{\delta F}{\delta n_e(r)}\frac{\partial n_e(r)}{\partial R}\right), \tag{B5}$$

where $\delta F/\delta n_q(r)$ and $\delta F/\delta n_e(r)$ denote the functional derivatives of $F$ with respect to the nucleon and electron densities, respectively.

Minimizing now the Helmholtz free energy $F$ with respect to arbitrary variations in $n_q(r)$ and $n_e(r)$ leads to the Euler-Lagrange equations

$$\lambda_q = \frac{\delta F}{\delta n_q(r)} \tag{B6a}$$

and

$$\lambda_e = \frac{\delta F}{\delta n_e(r)}, \tag{B6b}$$

where the $\lambda_q$ and $\lambda_e$ are Lagrange multipliers introduced to ensure that the nucleon and electron numbers given by Eqs. (B4a) and (B4b) remain fixed; they are identified with the corresponding chemical potentials. Using next the identities

$$\int_0^R dr\, r^2 \frac{\partial n_q(r)}{\partial R} = -R^2 n_q(R) \tag{B7a}$$

and

$$\int_0^R dr\, r^2 \frac{\partial n_e(r)}{\partial R} = -R^2 n_e(R), \tag{B7b}$$

which follow from the differentiation of Eqs. (B4a) and (B4b), respectively, we arrive at

$$P = -\mathcal{F}(R) + \lambda_e n_e(R) + \sum_q \lambda_q n_q(R). \tag{B8}$$

This pressure formula is a generalization of the expression derived in atomic physics in the framework of the Thomas-Fermi-Dirac model (see, e.g., Ref. [38] and references therein).

We decompose now the total Helmholtz free-energy density in the WS cell into a nuclear part, a purely kinetic electron part, and a Coulomb part,

$$\mathcal{F}(r) = \mathcal{F}_{\rm nuc}(r) + \mathcal{F}_e(r) + \mathcal{F}_{\rm Coul}(r). \tag{B9}$$

Then substituting Eq. (B9) into Eq. (B8) leads to

$$P = -\mathcal{F}_{\rm nuc}(R) - \mathcal{F}_e - \mathcal{F}_{\rm Coul}(R) + \lambda_e n_e + \sum_q \lambda_q n_q(R), \tag{B10}$$

where we are assuming that $n_e$ and $\mathcal{F}_e$ are position-independent. We now examine in more detail the different components of $\mathcal{F}(r)$ appearing in Eq. (B9).

In the fourth-order ETF method with Skyrme functionals the nuclear part $\mathcal{F}_{\rm nuc}(r)$ is a local functional of the nucleon densities $n_q(r)$ and their derivatives up to just the second order, provided the higher-order terms have been integrated as described in Sec. II. Note that we have *not* included the proton-proton Coulomb interaction in $\mathcal{F}_{\rm nuc}(r)$. For the electron gas, since it is supposed to be uniform we can write simply

$$F_e = V\mathcal{F}_e(n_e, T), \tag{B11}$$

where $\mathcal{F}_e$ is the electron Helmholtz free-energy density, which depends only on the electron density $n_e = N_p/V = \bar{n}_p$ and the temperature $T$. The Coulomb part of the Helmholtz free

energy is given by

$$F_{\rm Coul} = F_{\rm Coul,dir} + F_{\rm Coul,ex} = 4\pi \int_0^R dr\, r^2 \Big[ \mathcal{F}_{\rm Coul,dir}(r) + \mathcal{F}_{\rm Coul,ex}(r) \Big]. \quad \text{(B12)}$$

Here the direct term is

$$\mathcal{F}_{\rm Coul,dir}(r) = \frac{e}{2} n_c(r) \phi(r), \quad \text{(B13)}$$

where $n_c(r) \equiv n_p(r) - n_e$ is the net electric-charge density, and $\phi(r)$ is the Coulomb potential, found on solving Poisson's equation to be given by

$$\phi(r) = 4\pi e \int_0^R dr'\, r'^2 n_c(r') \mathcal{K}(r, r'), \quad \text{(B14)}$$

in which

$$\mathcal{K}(r, r') = \frac{r + r' - |r - r'|}{2rr'}. \quad \text{(B15)}$$

For $r = R$, Eq. (B14) reduces to

$$\phi(R) = \frac{4\pi e}{R} \int_0^R dr\, r^2 n_c(r) = 0, \quad \text{(B16)}$$

the last step being a consequence of global charge neutrality. It then follows from Eq. (B13) that

$$\mathcal{F}_{\rm Coul,dir}(R) = 0. \quad \text{(B17)}$$

For the Coulomb exchange term we have

$$\mathcal{F}_{\rm Coul,ex}(r) = -\frac{3e^2}{4} \left( \frac{3}{\pi} \right)^{1/3} \left[ x n_p(r)^{4/3} - \frac{1}{2} n_e^{4/3} \right], \quad \text{(B18)}$$

where $x$ is usually equal to 1 but, as explained in Sec. II, is set equal to zero for the BSk forces of this paper; for the electrons we have taken the extreme relativistic expression [32]. Then

$$\mathcal{F}_{\rm Coul}(R) = -\frac{3e^2}{4} \left( \frac{3}{\pi} \right)^{1/3} \left[ x n_p(R)^{4/3} - \frac{1}{2} n_e^{4/3} \right]. \quad \text{(B19)}$$

To proceed we have to evaluate the chemical potentials appearing in Eq. (B10). The Euler-Lagrange equation (B6a) for nucleons can be written explicitly as

$$\lambda_q = \frac{\partial \mathcal{F}_{\rm nuc}(r)}{\partial n_q(r)} - \nabla \cdot \frac{\partial \mathcal{F}_{\rm nuc}(r)}{\partial \nabla n_q(r)} + \nabla^2 \frac{\partial \mathcal{F}_{\rm nuc}(r)}{\partial \nabla^2 n_q(r)} + \left[ e\phi(r) - x e^2 \left( \frac{3}{\pi} \right)^{1/3} n_p(r)^{1/3} \right] \delta_{q,p}. \quad \text{(B20)}$$

The constant $\lambda_q$ can be evaluated at any point $r \leqslant R$, but taking $r = R$ leads to a considerable simplification of the right-hand side of Eq. (B20), since with our parametrization all derivatives of the density vanish at that point. Thus the second and third terms of this expression likewise vanish at that point, since each can be expressed as a sum of terms every one of which contains a factor of some derivative of $n_q(r)$. By using then Eq. (B16) the nucleon chemical potential becomes

$$\lambda_q = \frac{\partial \mathcal{F}_{\rm nuc}(R)}{\partial n_q(R)} - x e^2 \left( \frac{3}{\pi} \right)^{1/3} n_p(R)^{1/3} \delta_{q,p}. \quad \text{(B21)}$$

A further consequence of the vanishing of the derivatives of $n_q(r)$ at $r = R$ is that the first term here, like the term $\mathcal{F}_{\rm nuc}(R)$ appearing in Eq. (B10), involves only the bulk part of the nuclear free-energy density. Next, the Euler-Lagrange equation (B6b) for electrons simplifies to

$$\lambda_e = \frac{\partial \mathcal{F}_e}{\partial n_e} - e\phi(r) + \frac{e^2}{2} \left( \frac{3}{\pi} \right)^{1/3} n_e^{1/3}, \quad \text{(B22)}$$

because of the uniformity of the electron gas. For the same reason we can write the electron pressure (without the Coulomb exchange term) as

$$P_e = -\frac{\partial F_e}{\partial V} = -\mathcal{F}_e + n_e \frac{\partial \mathcal{F}_e}{\partial n_e}. \quad \text{(B23)}$$

Also, the Coulomb-potential term $e\phi(r)$ in Eq. (B22) vanishes at $r = R$, and it must be negligible for $r < R$, since otherwise $n_e$ and $\mathcal{F}_e$ would be position-dependent, which would be inconsistent with the assumption made and justified in Sec. II that the electron gas is essentially uniform in the inner crust. Then Eq. (B22) can be rewritten as

$$\lambda_e n_e = P_e + \mathcal{F}_e + \frac{e^2}{2} \left( \frac{3}{\pi} \right)^{1/3} n_e^{1/3}. \quad \text{(B24)}$$

Substituting now Eqs. (B19), (B21), and (B24) into Eq. (B10) gives us for the total pressure

$$P = P_{\rm nuc} + P_e + P_{\rm Coul,ex}, \quad \text{(B25)}$$

where

$$P_{\rm nuc} = -\mathcal{F}_{\rm nuc}(R) + \sum_q n_q(R) \frac{\partial \mathcal{F}_{\rm nuc}(R)}{\partial n_q(R)} \quad \text{(B26)}$$

and

$$P_{\rm Coul,ex} = \frac{e^2}{8} \left( \frac{3}{\pi} \right)^{1/3} n_e^{4/3} - x \frac{e^2}{4} \left( \frac{3}{\pi} \right)^{1/3} n_p(R)^{4/3}. \quad \text{(B27)}$$

Given that both terms on the right-hand side of Eq. (B26) relate only to bulk matter, being independent of any density-gradient terms, it is easy to show from Eq. (B1) that $P_{\rm nuc}$ represents the purely nuclear pressure of homogeneous nuclear matter with neutron and proton densities equal to $n_n(R)$ and $n_p(R)$, respectively, without any Coulomb term, direct or exchange. However, from Eq. (B18) it is seen that the last term of Eq. (B27) is just the Coulomb exchange pressure associated with the protons of this homogeneous system, while the first term of this equation is likewise the Coulomb exchange pressure of the uniform electron gas.

This means that the pressure of any crustal layer is the same as that obtained in a homogeneous medium of neutrons, protons, and electrons, with the neutron and proton densities being those found at the surface of the WS cell, i.e., in the homogeneous background, $n_{Bn}$ and $n_{Bp}$, respectively, while the electron density is to be taken as that of the actual uniform electron gas, $n_e$. It is remarkable that the direct Coulomb contribution, calculated exactly, vanishes identically, even though $n_p(R)$ is not equal to $n_e$. However, this term still manifests itself indirectly, since it influences the actual values of $n_n(R)$ and $n_p(R)$ through the Euler-Lagrange equations. A similar remark applies also to the inhomogeneities inside the cell.

For the generalized Skyrme force (1), the purely nuclear pressure can be expressed as

$$P_{\rm nuc} = \frac{\hbar^2}{3M}\tau_0 + \sum_{t=0,1}\left(C_t^n n_{Bt}^2 + \frac{5}{3}C_t^\tau n_{Bt}\tau_t + n_{B0}\frac{\partial C_t^n}{\partial n_{B0}}n_{Bt}^2 + n_{B0}\frac{\partial C_t^\tau}{\partial n_{B0}}n_{Bt}\tau_t\right), \tag{B28}$$

where $n_{B0} = n_{Bn} + n_{Bp}$, while $n_{B1} = n_{Bn} - n_{Bp}$, and likewise for $\tau_0$ and $\tau_1$, with

$$\tau_q = \tfrac{3}{5}(3\pi^2)^{2/3} n_q (R)^{5/3}. \tag{B29}$$

The various coefficients are given by

$$C_0^n = \tfrac{3}{8}t_0 + \tfrac{3}{48}t_3 n_{B0}^\alpha, \tag{B30a}$$

$$C_1^n = -\tfrac{1}{4}t_0\left(\tfrac{1}{2}+x_0\right) - \tfrac{1}{24}t_3(1+x_3)n_{B0}^\alpha, \tag{B30b}$$

$$C_0^\tau = \tfrac{3}{16}t_1 + \tfrac{1}{4}t_2\left(\tfrac{5}{4}+x_2\right) + \tfrac{3}{16}t_4 n_{B0}^\beta + \tfrac{1}{4}t_5\left(\tfrac{5}{4}+x_5\right)n_{B0}^\gamma, \tag{B30c}$$

$$C_1^\tau = -\tfrac{1}{8}t_1\left(\tfrac{1}{2}+x_1\right) + \tfrac{1}{8}t_2\left(\tfrac{1}{2}+x_2\right) - \tfrac{1}{8}t_4 n_{B0}^\beta\left(\tfrac{1}{2}+x_4\right) + \tfrac{1}{8}t_5 n_{B0}^\gamma\left(\tfrac{1}{2}+x_5\right). \tag{B30d}$$

The pressure $P_e$ of the uniform electron gas is calculated as described in Sec. II, using expressions given in Sec. 24 of Cox and Giuli [30].


[1] C. J. Pethick and D. G. Ravenhall, Annu. Rev. Nucl. Part. Sci. **45**, 429 (1995).
[2] N. Chamel and P. Haensel, Living Rev. Relativity **11**, 10 (2008) [http://www.livingreviews.org/lrr-2008-10].
[3] S. Goriely, N. Chamel, and J. M. Pearson, Phys. Rev. C **82**, 035804 (2010).
[4] N. Chamel, Phys. Rev. C **82**, 014313 (2010).
[5] N. Chamel and S. Goriely, Phys. Rev. C **82**, 045804 (2010).
[6] G. Audi, A. H. Wapstra, and C. Thibault, Nucl. Phys. A **729**, 337 (2003).
[7] J. M. Pearson, S. Goriely, and N. Chamel, Phys. Rev. C **83**, 065810 (2011).
[8] E. Chabanat, P. Bonche, P. Haensel, J. Meyer, and R. Schaeffer, Nucl. Phys. A **635**, 231 (1998); **643**, 441 (1998).
[9] S. Goriely, M. Samyn, J. M. Pearson, and M. Onsi, Nucl. Phys. A **750**, 425 (2005).
[10] J. Dobaczewski, M. V. Stoitsov, and W. Nazarewicz, AIP Conf. Proc. **726**, 51 (2004).
[11] J. W. Negele and D. Vautherin, Nucl. Phys. A **207**, 298 (1973).
[12] J. Margueron, N. van Giai, and N. Sandulescu, in *Proceedings of the International Symposium EXOCT07*, edited by U. Lombardo, M. Baldo, F. Burgio, and H.-J. Schulze (World Scientific, Singapore, 2008), p. 362.
[13] N. Chamel, S. Naimi, E. Khan, and J. Margueron, Phys. Rev. C **75**, 055806 (2007).
[14] F. Grill, J. Margueron, and N. Sandulescu, Phys. Rev. C **84**, 065801 (2011).
[15] P. Magierski and P.-H. Heenen, Phys. Rev. C **65**, 045804 (2002).
[16] P. Gögelein and H. Müther, Phys. Rev. C **76**, 024312 (2007).
[17] W. G. Newton and J. R. Stone, Phys. Rev. C **79**, 055801 (2009).
[18] F. Douchin and P. Haensel, Astron. Astrophys. **380**, 151 (2001).
[19] K. Oyamatsu and K. Iida, Phys. Rev. C **75**, 015801 (2007).
[20] M. Onsi, A. K. Dutta, H. Chatri, S. Goriely, N. Chamel, and J. M. Pearson, Phys. Rev. C **77**, 065805 (2008).
[21] M. Onsi, H. Przysiezniak, and J. M. Pearson, Phys. Rev. C **55**, 3139 (1997).
[22] K. Oyamatsu and M. Yamada, Nucl. Phys. A **578**, 181 (1994).
[23] N. Chamel, Nucl. Phys. A **773**, 263 (2006).
[24] R. C. Tolman, Phys. Rev. **55**, 364 (1939).
[25] J. R. Oppenheimer and G. M. Volkoff, Phys. Rev. **55**, 374 (1939).
[26] N. Chamel, S. Goriely, and J. M. Pearson, Phys. Rev. C **80**, 065804 (2009).
[27] M. Brack, C. Guet, and H.-B. Håkansson, Phys. Rep. **123**, 275 (1985).
[28] G. Watanabe and K. Iida, Phys. Rev. C **68**, 045801 (2003).
[29] T. Maruyama, T. Tatsumi, D. N. Voskresensky, T. Tanigawa, and S. Chiba, Phys. Rev. C **72**, 015802 (2005).
[30] A. Weiss, W. Hillebrandt, H.-C. Thomas, and H. Ritter, *Cox and Giuli's Principles of Stellar Structure*, extended 2nd ed. (Cambridge Scientific, Cottenham, UK, 2004).
[31] S. Goriely and J. M. Pearson, Phys. Rev. C **77**, 031301(R) (2008).
[32] E. Salpeter, Astrophys. J. **134**, 669 (1961).
[33] C. Ducoin, Ph. Chomaz, and F. Gulminelli, Nucl. Phys. A **789**, 403 (2007).
[34] F. Douchin and P. Haensel, Phys. Lett. B **485**, 107 (2000).
[35] [http://phys-merger.physik.unibas.ch/~hempel/eos/oc/sly4.eos].
[36] S. B. Rüster, M. Hempel, and J. Schaffner-Bielich, Phys. Rev. C **73**, 035804 (2006).
[37] S. L. Shapiro and S. A. Teukolsky, *Black Holes, White Dwarfs, and Neutron Stars* (Wiley Interscience, New York, 1983).
[38] A. M. Abrahams and S. L. Shapiro, Phys. Rev. A **42**, 2530 (1990).
[39] N. Chamel, A. F. Fantina, J. M. Pearson, and S. Goriely, Phys. Rev. C **84**, 062802 (2011).